

Electronic Supplementary Materials

Heterostructuring Cobalt Sulfide with Highly Oxophilic 1T-Tungsten Sulfide for Durable and Efficient Oxygen Electrocatalysis

Shengxiong Yang,^a Bin Li,^a Minqiu Lan,^a Liangsheng Liu,^a Yimin Sun,^c Fei Xiao,^{a, b} Junwu Xiao^{a, *}

^aKey Laboratory of Material Chemistry for Energy Conversion and Storage, Ministry of Education, Hubei Key Laboratory of Material Chemistry and Service Failure, Department of Chemistry and Chemical Engineering, Huazhong University of Science & Technology, Wuhan 430074, China.

^bShenzhen Huazhong University of Science and Technology Research Institute, Shenzhen 518000, China

^cHubei key Laboratory of Plasma Chemistry and Advanced Materials, School of Materials Science and Engineering, Wuhan Institute of Technology, 693 Xiongchu Avenue, Wuhan, 430073, China

E-mail: chjwxiao@hust.edu.cn

Materials characterization

The structures of the samples were characterized on FEI Nova NanoSEM 450 Scanning Electron Microscope (SEM) and Tecnai G2 20 Transmission Electron Microscopy (TEM). The composition and chemical states of the samples were analyzed on Philips PW-1830 X-ray diffractometer, Agilent 4100 Microwave Plasma-Atom Emission Spectrometer (MP-AES), and a PHI 5600 X-ray photoelectron spectroscopy (XPS) system. The oxygen temperature-programmed desorption (O₂-

TPD) profiles were recorded on a VDSorb-91i (Vodo) chemical adsorption analyzer. 100 mg of the samples were first annealed at 300 °C for 30 min and then cooled to 30 °C at a He flow rate of 15 sccm, and were exposed in He gas containing 5 % O₂ for 30 min at 30 °C, followed by being purged by He gas for 30 min. It was then raised to 600 °C with a ramping rate of 10 °C min⁻¹ at a He flow rate of 15 sccm.

Electrochemical characterization

Electrochemical oxygen reduction reaction tests

The ORR performances in the rotating disk electrode (RDE) setup were performed in 0.1 M KOH solution using a IVIUM Verter potentiostat and RRDE-3A rotating ring-disk electrode system. Depositing 5 μL of the ink that was prepared via ultrasonically dispersing 5.0 mg of catalyst into 990 N, N-Dimethylformamide (DMF) with 10 μL Nafion solution (5 wt%) on a polished glassy carbon (GC) rotating-disk electrode (4 mm in diameter) is employed as the working electrode. The catalyst loading in the WE is ~ 0.2 mg cm⁻² for PGM free catalysts and 40 μg_{Pt} cm⁻² for Pt/C catalyst (20 wt%, Johnson Matthey). Graphitic rod was used as counter electrode (CE), and were and reference electrode (RE), respectively. All potentials were recorded versus Hg/HgO reference electrode (0.098 V versus standard hydrogen electrode), and were reported versus the reversible hydrogen electrode (RHE) based on the Nernst equation: $E(RHE) = E(Hg/HgO) + 0.098 + 0.0591 \times pH(V)$. During the rotating-ring disk electrode (RRDE) experiment, the disk electrode scanned cathodically from 1.0 V to 0.4 V versus RHE, and the Pt ring set as 1.2 V versus RHE. The turn-over frequency (TOF) for the ORR is calculated according to the equation below:

$$TOF = \frac{J_{0.80} \times M_w}{4 \times F \times m \times W} \quad (1)$$

where $J_{0.80}$ is the kinetic current density (mA cm^{-2}) at 0.80 V versus RHE, M_w is molar mass of Co (58.7 g mol^{-1}) or Pt (195.1 g mol^{-1}), m is the catalyst loading (mg cm^{-2}) in the RDE, W is the mass percentage of Co or Pt in the catalysts, F is the Faraday constant (96485 C mol^{-1}).

The ORR performance in the gas diffusion electrode (GDE) setup was carried out on a IVIUM Verter potentiostat and home-made half-cell system at $25 \text{ }^\circ\text{C}$. The catalyst ink that was prepared via ultrasonically dispersing catalyst powder into water-isopropanol (1:4 m/m) with the addition of PiperION (5 wt% in ethanol, Versogen) ionomer was deposited onto Sigracet SGL 29 BC gas diffusion layer through the airbrush spraying method as the WE. The area and catalyst loading in the WE were 5 cm^2 and 2.0 mg cm^{-2} . The Pt mesh counter electrode and Hg/HgO reference electrode were inserted into a $25 \times 25 \times 8 \text{ mm}$ pore at the center of grooved Teflon plate filled by 1.0 M KOH solution. They were assembled into half-cell gas diffusion electrode, coupled to a PiperION anion exchange membrane, polytetrafluoroethylene (PTFE) gasket, graphite bipolar plate, as well as gold-coated current collector. Oxygen gas with a relative humidity of 100 % was fed into catalyst layer via graphite bipolar plate and gas diffusion layer at 100 sccm.

Electrochemical oxygen evolution reaction tests

The OER performances were executed on a IVIUM Verter potentiostat and L-shaped glassy carbon electrode (4 mm in diameter). The LSV curves of the samples were recorded in O_2 -saturated 1.0 M KOH solution at a scan rate of 5 mV s^{-1} with 85 %- iR compensation. The electrochemically active surface areas (ECSA) of the samples were tested in N_2 -saturated 1.0 M KOH solution using cyclic voltammetry (CV) method. Electrochemical impedance spectroscopy (EIS) was recorded at an OER potential of 1.65 V versus RHE with a 10 mV AC amplitude and in a frequency of 100 kHz-0.1

Hz. The TOF for the OER was obtained from the equation 2:

$$TOF = \frac{J_{1.65} \times M_{Co}}{4 \times F \times m \times W} \quad (2)$$

where $J_{1.65}$ is an OER current density (mA cm^{-2}) at 1.65 V versus RHE, M_{Co} is molar mass of Co (58.7 g mol^{-1}), m is the catalyst loading (mg cm^{-2}) in L-shaped glassy carbon electrode, W is the mass percentage of cobalt in the catalysts, F is the Faraday constant (96485 C mol^{-1}).

Rechargeable zinc-air battery

The zinc-air battery was composed of a polished zinc anode, the 6.0 M KOH and 0.2 M $\text{Zn}(\text{Ac})_2$ electrolyte, and air cathode. The air cathode was fabricated via spraying catalyst ink on a nickel foam and hydrophobic carbon fiber paper current collector. The catalyst loading is $\sim 2.5 \text{ mg cm}^{-2}$. Catalyst layer deposited on nickel foam was located at water-facing side, and hydrophobic carbon fiber paper was placed at the air-facing side. The catalyst ink was prepared via the similar approach to that for the electrochemical characterization. The Pt/C+ RuO_2 cathode with a loading of 2.5 mg cm^{-2} was prepared via mixing 2.5 mg Pt/C (20 wt%) and 2.5 mg RuO_2 powders for comparison. The battery performance was measured on a IVIUM Verter potentiostat and LAND-V34 battery test system. The discharge polarization curves were recorded at 5 mV s^{-1} using LSV method. The cycle life was tested using galvanostatic pluse method, where the battery was charged for 10 min per cycle at 5 mA cm^{-2} , followed by 10 min of discharging at 5 mA cm^{-2} .

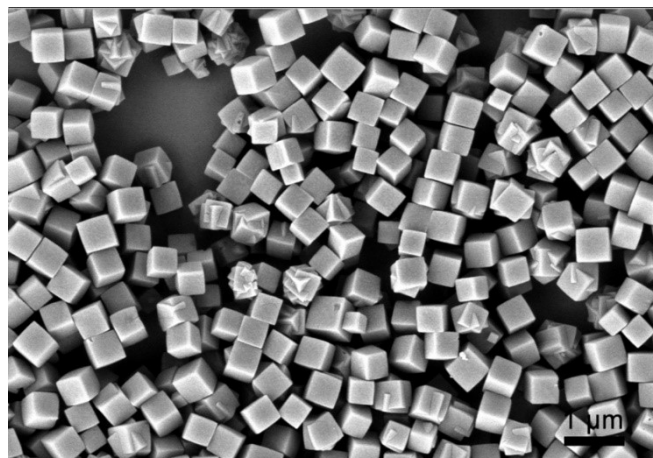


Figure S1. SEM image of ZIF-67 nanocubes.

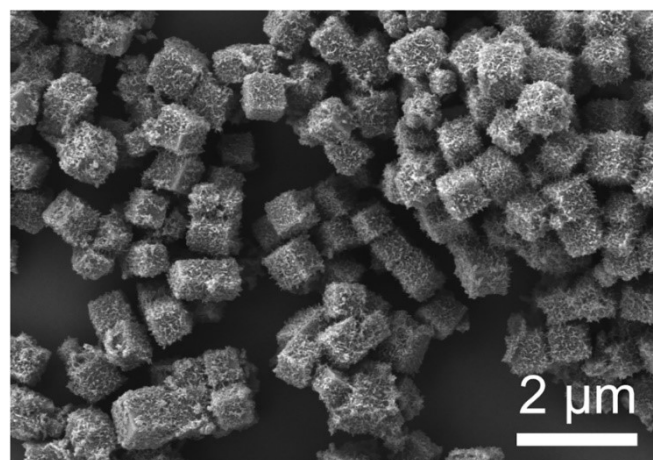


Figure S2. SEM image of ZIF-67/PmAP-HCO₃⁻ nanocubes.

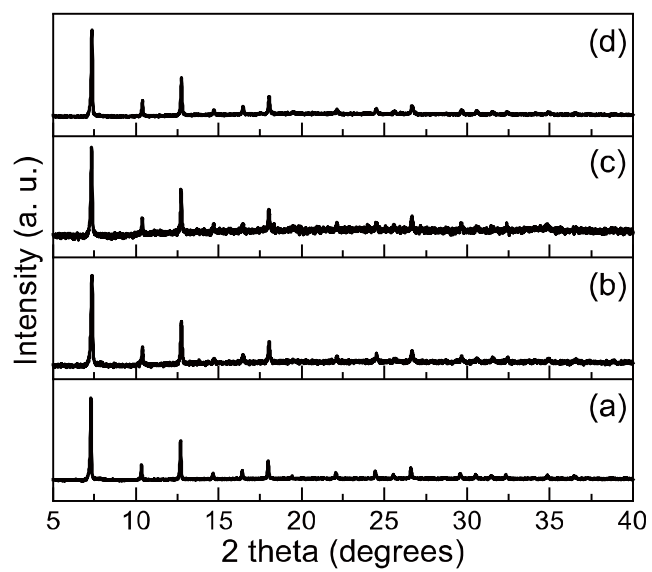


Figure S3. XRD patterns of (a) ZIF-67, (b) ZIF-67/*Pm*AP-HCO₃⁻, (c) ZIF-67/*Pm*AP-HCO₃⁻/WO₄²⁻, and (d) ZIF-67/*Pm*AP-WO₄²⁻.

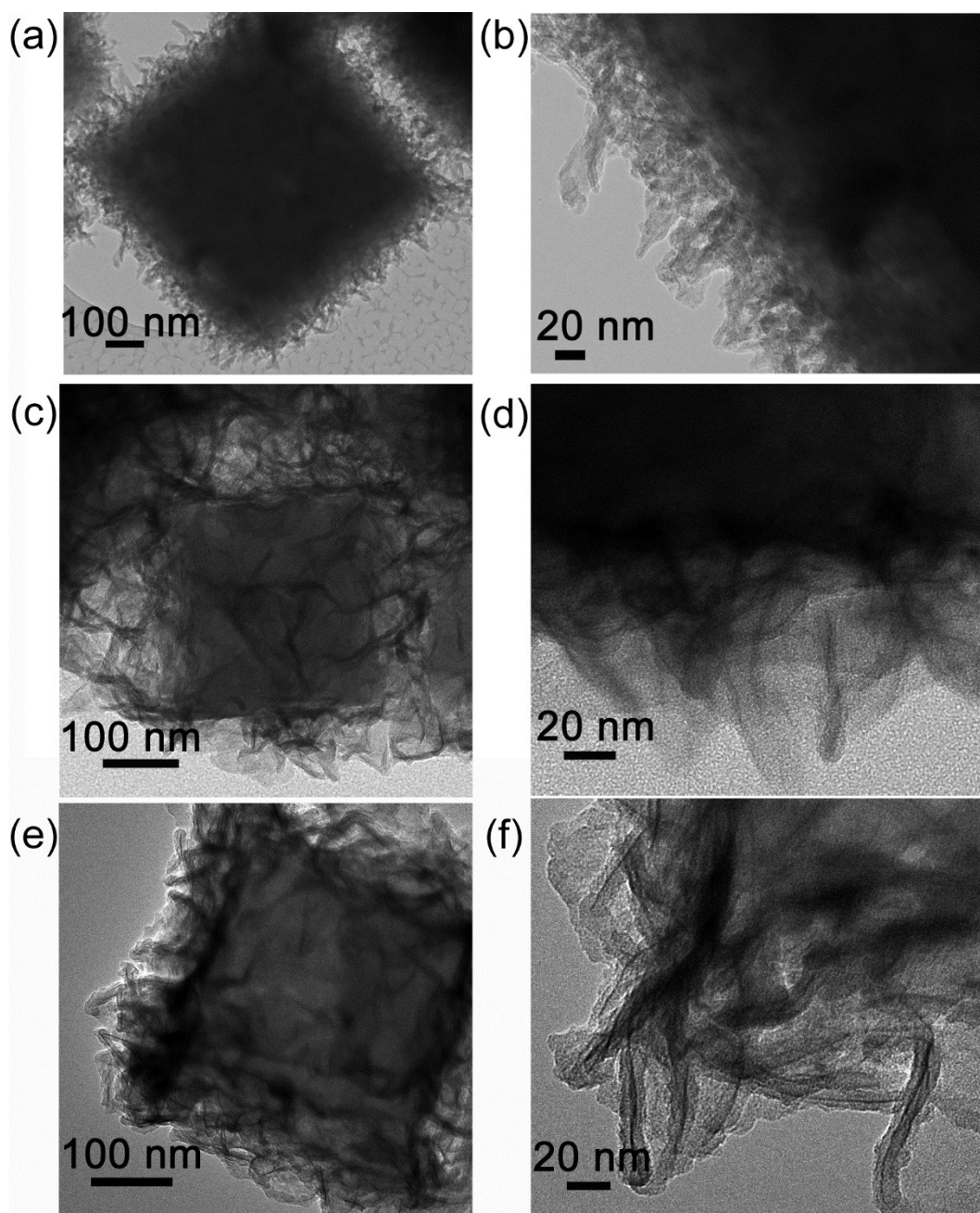


Figure S4. TEM and high-magnification TEM images of (a and b) ZIF-67/PmAP-HCO₃⁻, (c and d) ZIF-67/PmAP-HCO₃⁻/WO₄²⁻, and (e and f) ZIF-67/PmAP-WO₄²⁻.

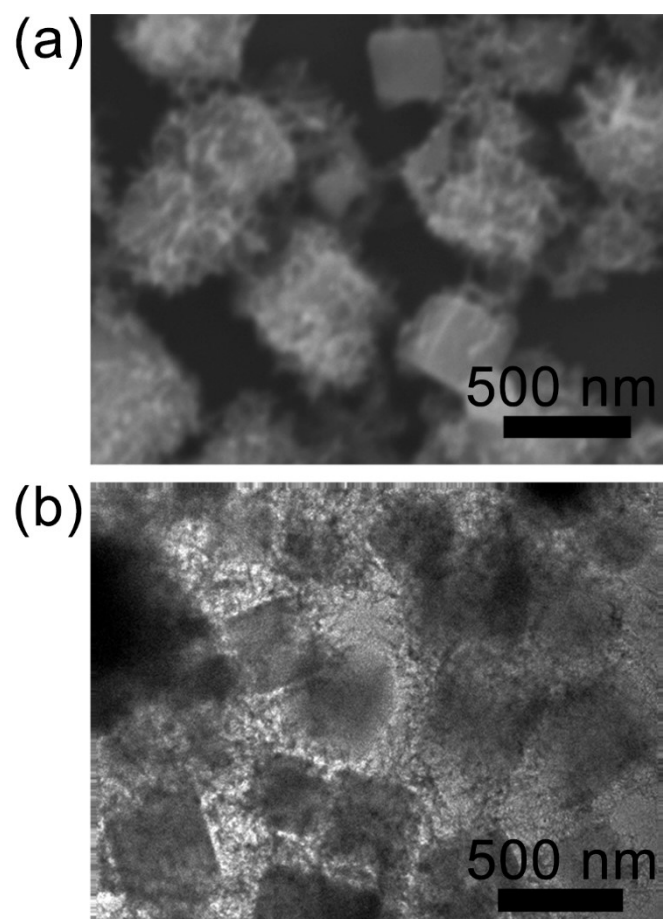


Figure S5. (A) SEM and (B) TEM images of ZIF-67/HCO₃⁻.

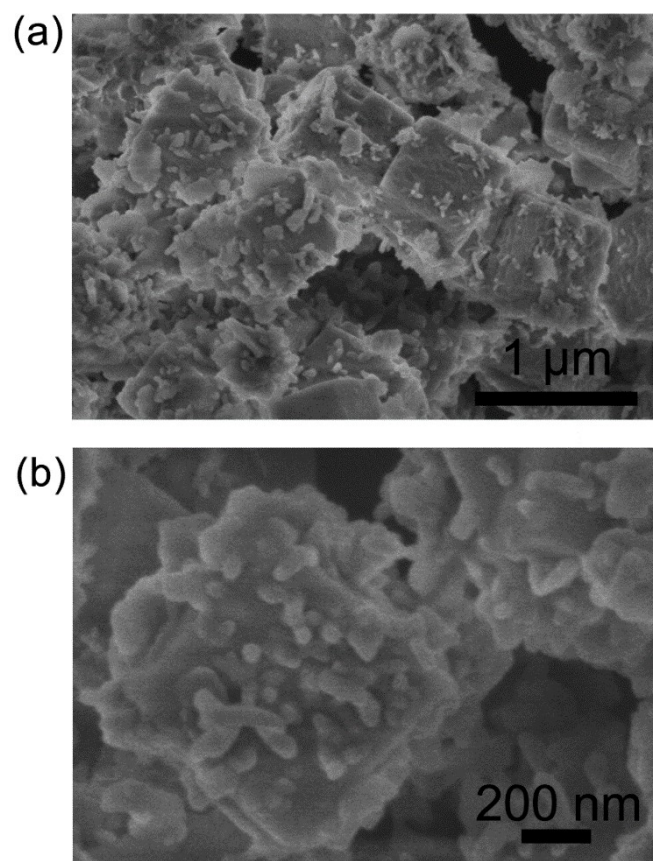


Figure S6. (a) SEM and (b) high-magnification SEM images of ZIF-67/*PmAP*.

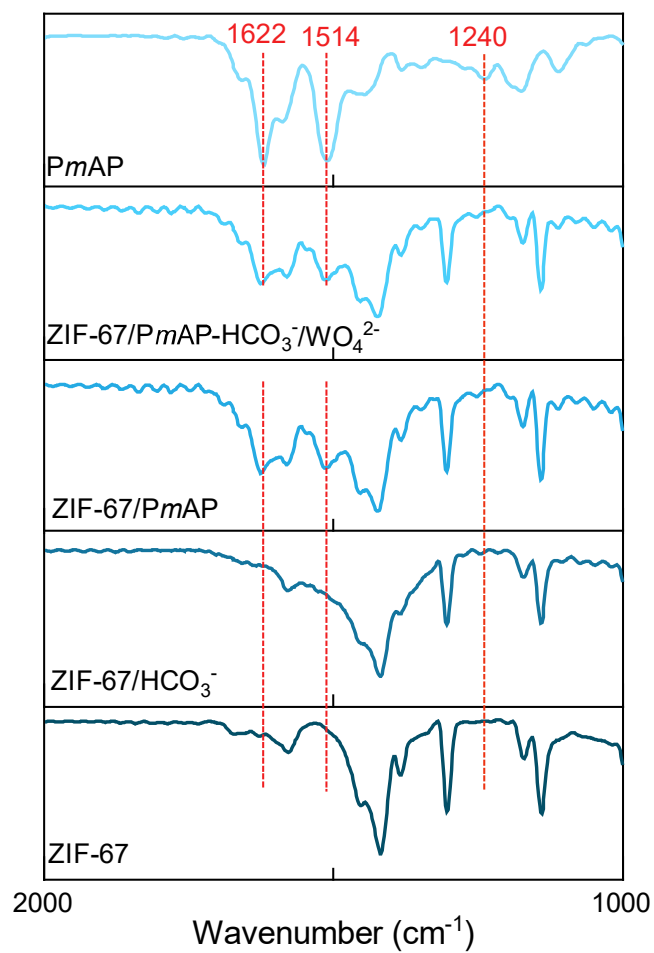


Figure S7. FT-IR spectra of ZIF-67, ZIF-67/HCO₃⁻, ZIF-67/PmAP, ZIF-67/PmAP-HCO₃⁻/WO₄²⁻, and PmAP.

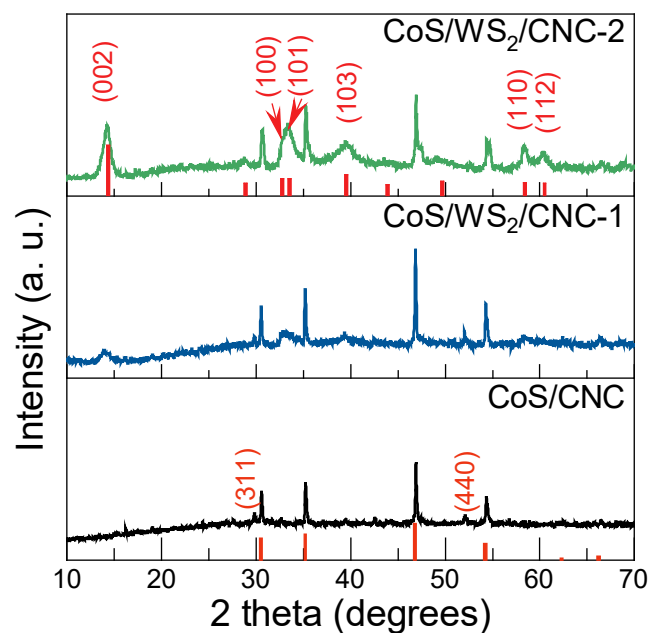


Figure S8. XRD of CoS/CNC, CoS/WS₂/CNC-1, and CoS/WS₂/CNC-2 obtained from the sulfurization of ZIF-67/PmAP-HCO₃⁻, ZIF-67/PmAP-HCO₃⁻/WO₄²⁻, and ZIF-67/PmAP-WO₄²⁻ precursors. The diffraction peaks at 29.8° and 52.1° correspond to the (311) and (440) planes of Co₉S₈ (JCPDS 03-065-1765). The diffraction peaks at 2θ=14.3°, 32.8°, 33.6°, 39.5°, 58.4°, and 60.5° belong to WS₂ phase (JCPDS 00-008-0237). The other peaks originate from CoS phase (JCPDS 01-070-2864).

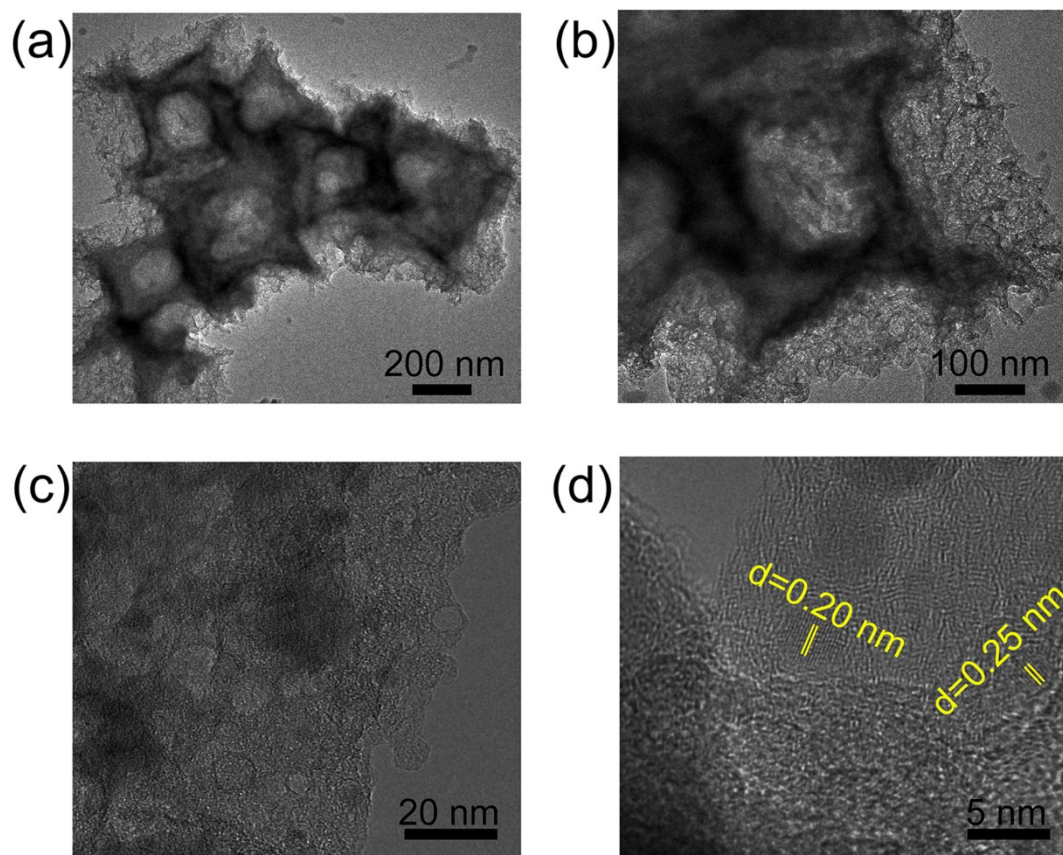


Figure S9. (a and b) Low-magnification TEM, (c) high-magnification TEM, and (d) high-resolution TEM images of CoS/CNC. The lattice distances at 0.20 nm and 0.25 nm are corresponding to (102) and (101) faces of CoS, respectively.

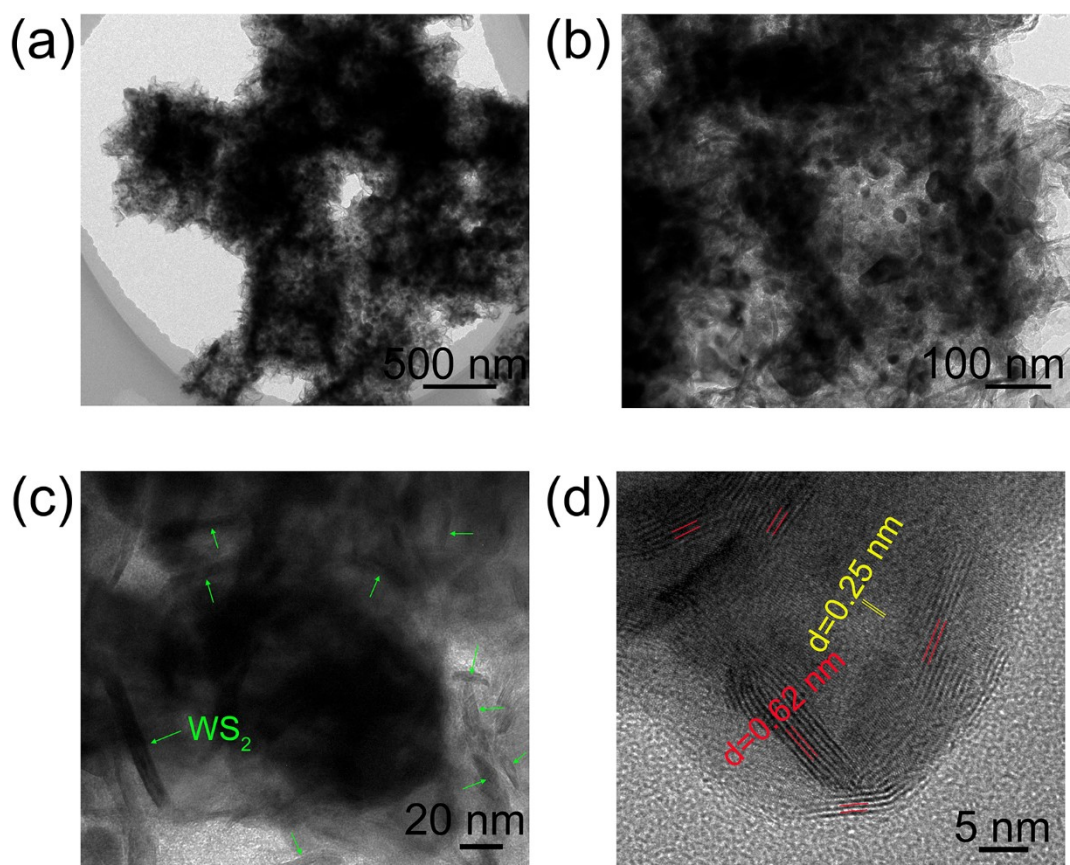


Figure S10. (a and b) Low-magnification TEM, (c) high-magnification TEM, and (d) HRTEM images of CoS/WS₂/CNC-2.

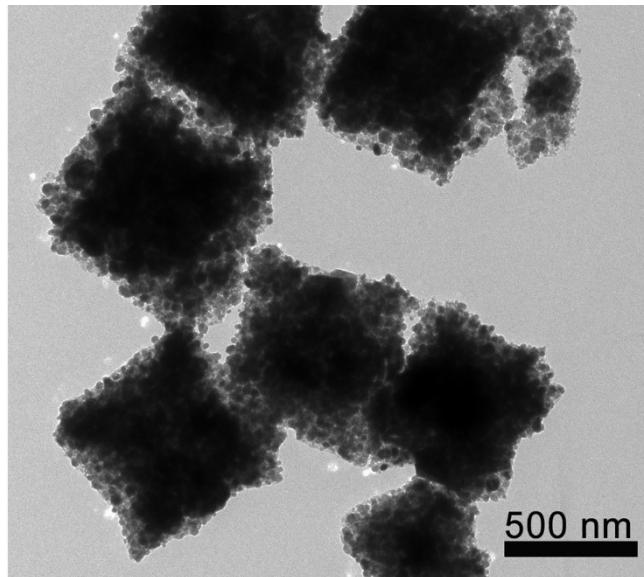


Figure S11. TEM image of ZIF-67-derived solid nanocubes via the similar sulfurization process.

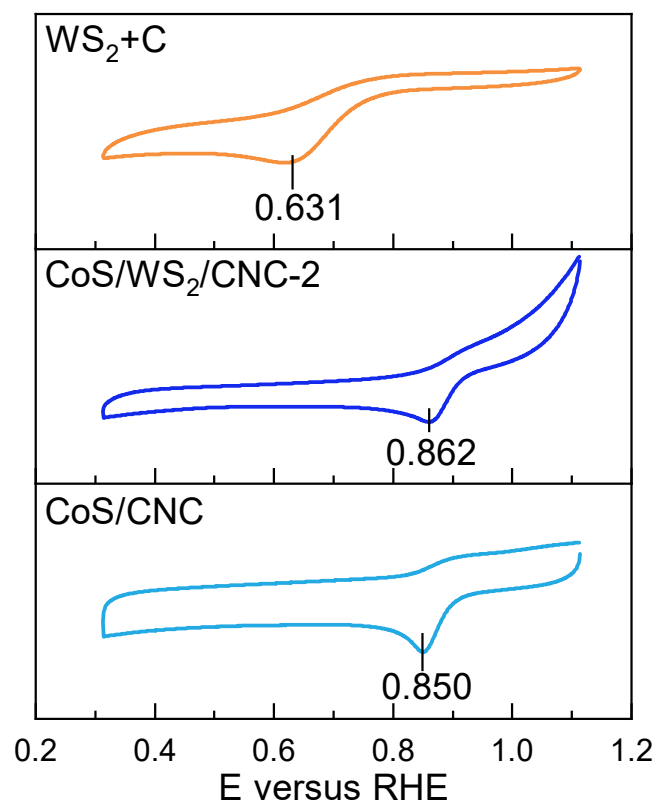


Figure S12. CV curves of carbon nanocubes-supported CoS, CoS/WS₂-2, and WS₂+C catalysts recorded in O₂-saturated 0.1 M KOH solution.

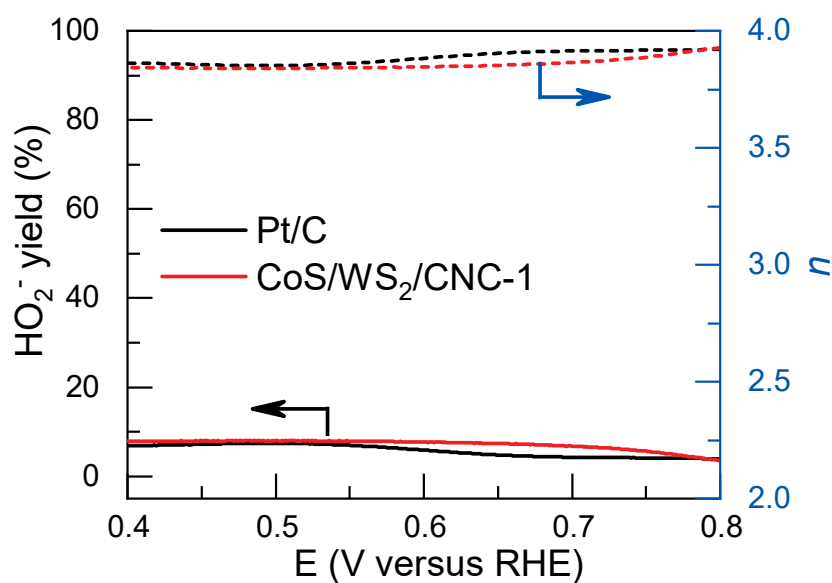


Figure S13. The HO₂⁻ yield and number of electron transferred for Pt/C and CoS/WS₂/CNC-1 catalysts

calculated from RRDE curves according to the following equations:

$$HO_2^- \% = \frac{200 \times I_r / N}{I_d + I_r / N} \quad [3]$$

$$n = \frac{4 \times I_d}{I_d + I_r / N} \quad [4]$$

Where I_d and I_r are the disk and ring currents, respectively. N is current collection efficiency (0.36) of Pt ring.

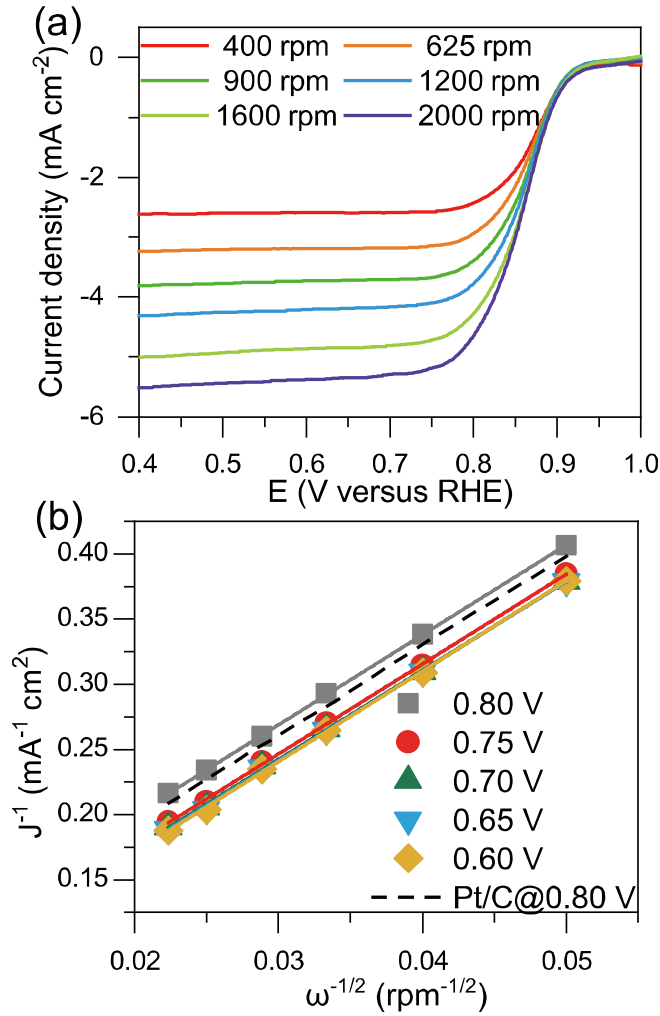


Figure S14. (a) LSV profiles of CoS/WS₂/CNC-1 recorded at a rotating speed of 2000-400 rpm, and

(b) Koutecky-Levich plots at the potentials of 0.80-0.60 V versus RHE that are calculated from LSV

curves on the basis of the following equations:

$$\frac{1}{J} = \frac{1}{J_k} + \frac{1}{J_L} = \frac{1}{J_k} + \frac{1}{B\omega^{1/2}} \quad [5]$$

$$B = 0.62nFC_oD_o^{2/3}\nu^{-1/6} \quad [6]$$

$$J_k = nFkC_o \quad [7]$$

Where J is the measured current density, J_k and J_L are the kinetic- and diffusion-limiting current

densities, ω is the angular velocity, n is transferred electron number, F is the Faraday constant (96485 C mol^{-1}), C_0 is the bulk concentration of O_2 ($1.2 \times 10^{-6} \text{ mol cm}^{-3}$), ν is the kinematic viscosity of the electrolyte ($0.01 \text{ cm}^2 \text{ s}^{-1}$), D_0 is the O_2 diffusion coefficient ($1.9 \times 10^{-5} \text{ cm}^2 \text{ s}^{-1}$), and k is the electron-transfer rate constant.

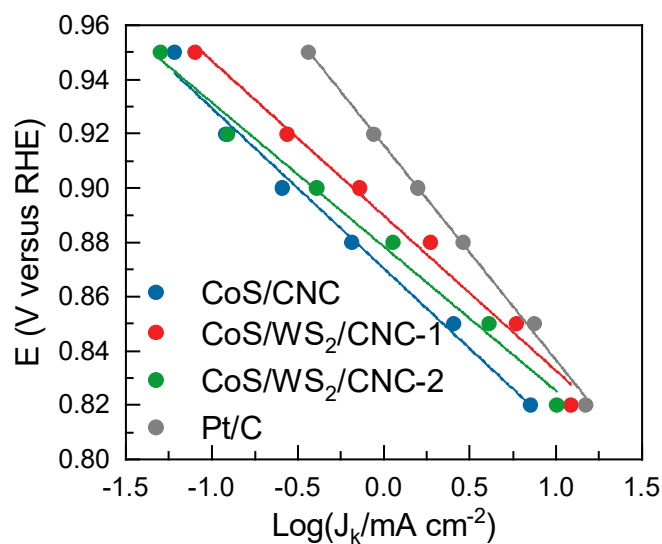


Figure S15. Tafel plots of CoS/CNC, CoS/WS₂/CNC-1, CoS/WS₂/CNC-2, and Pt/C catalysts.

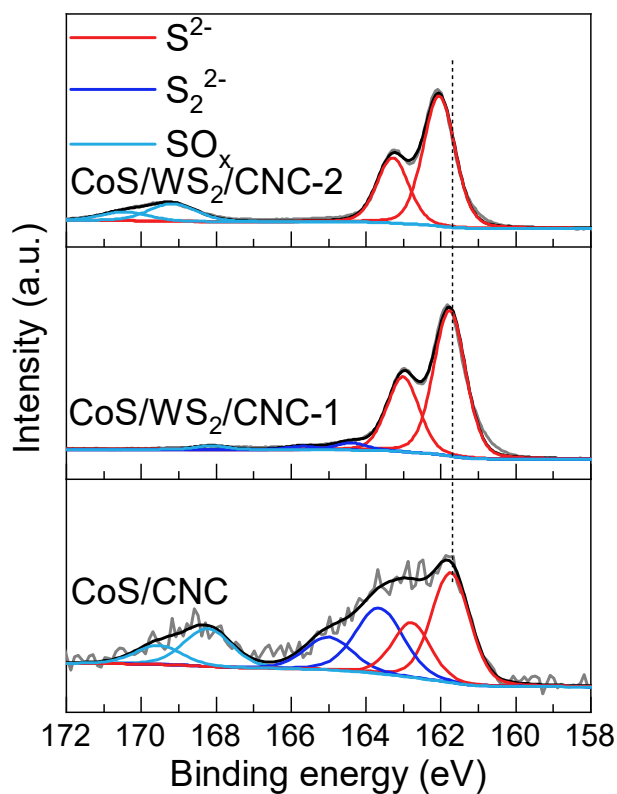


Figure S16. High-resolution S 2p XPS spectra of CoS/CNC, CoS/WS₂/CNC-1, and CoS/WS₂/CNC-2 catalysts.

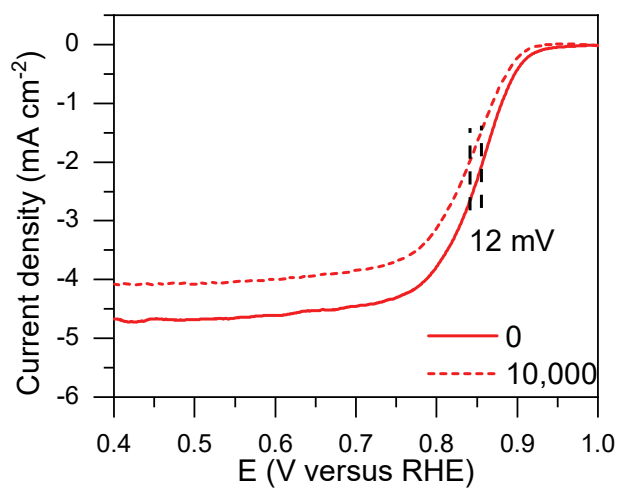


Figure S17. LSV curves of CoS/CNC catalysts recorded in O₂-saturated 0.1 M KOH solution before and after 10,000 ADT cycling.

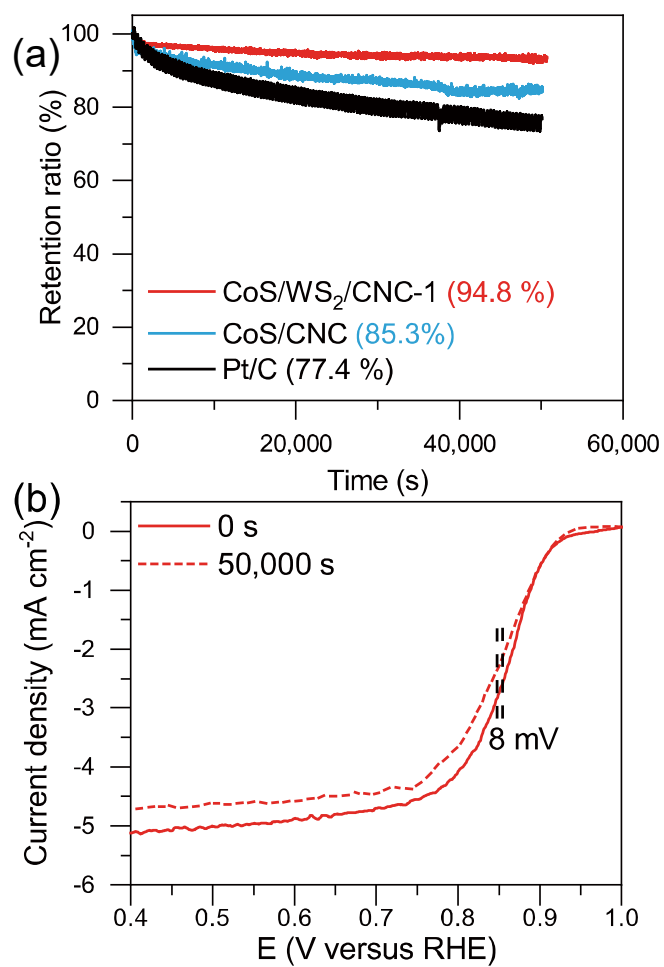


Figure S18. (a) Chronoamperometric Response of CoS/WS₂/CNC-1, CoS/CNC, and Pt/C at 0.5 V versus RHE. (b) LSV curves of CoS/WS₂/CNC-1 catalyst before and after 50,000 s operation at 0.5 V versus RHE.

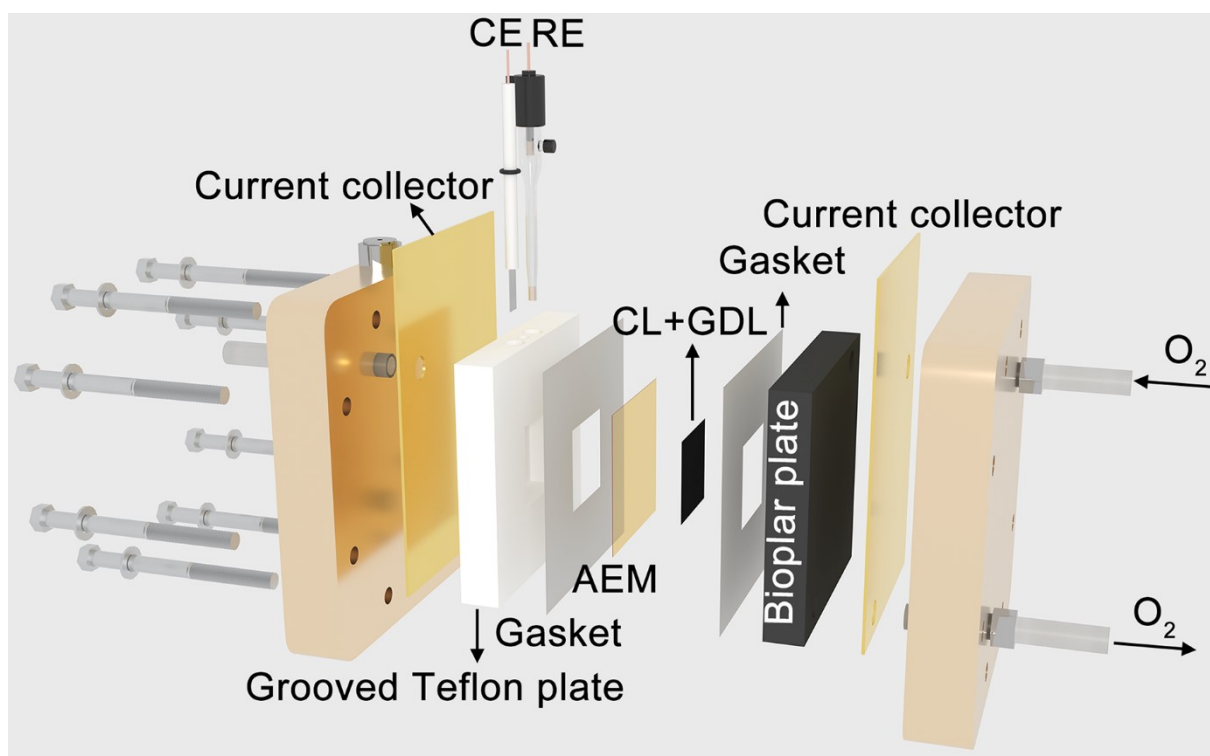


Figure S19. Schematically showing the structure of half-cell gas diffusion electrode (GDE) setup. (AEM: anion exchange membrane; CL: catalyst layer; GDL: gas diffusion layer; CE: counter electrode; RE: reference electrode)

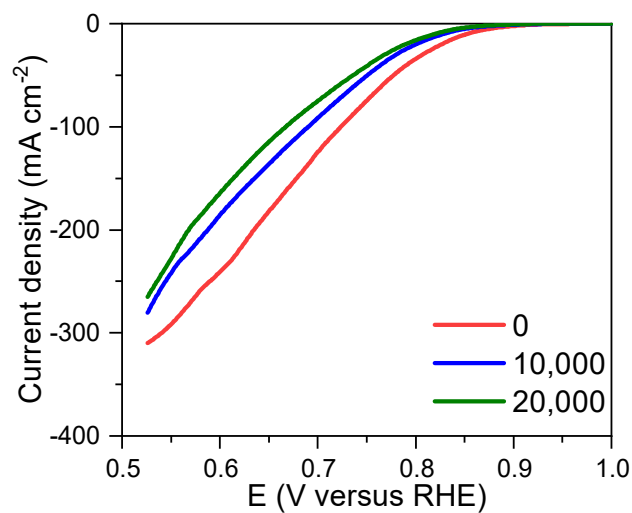


Figure S20. The ORR polarization curves of CoS/CNC catalyst in the GDE configuration during ADT cycling.

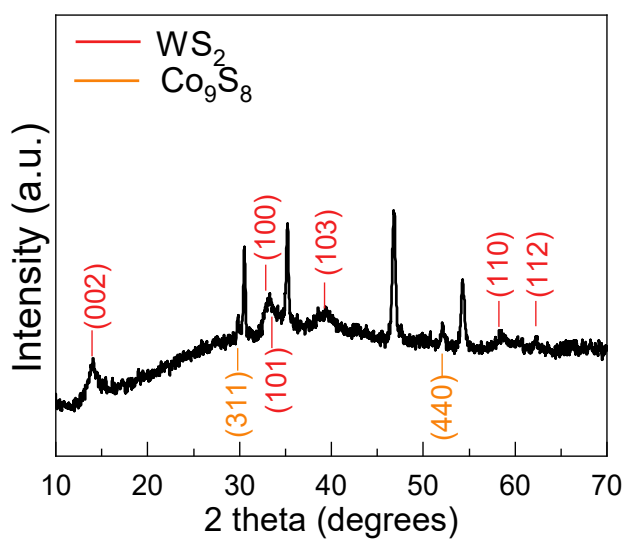


Figure S21. XRD pattern of CoS/WS₂/CNC-1-ADT.

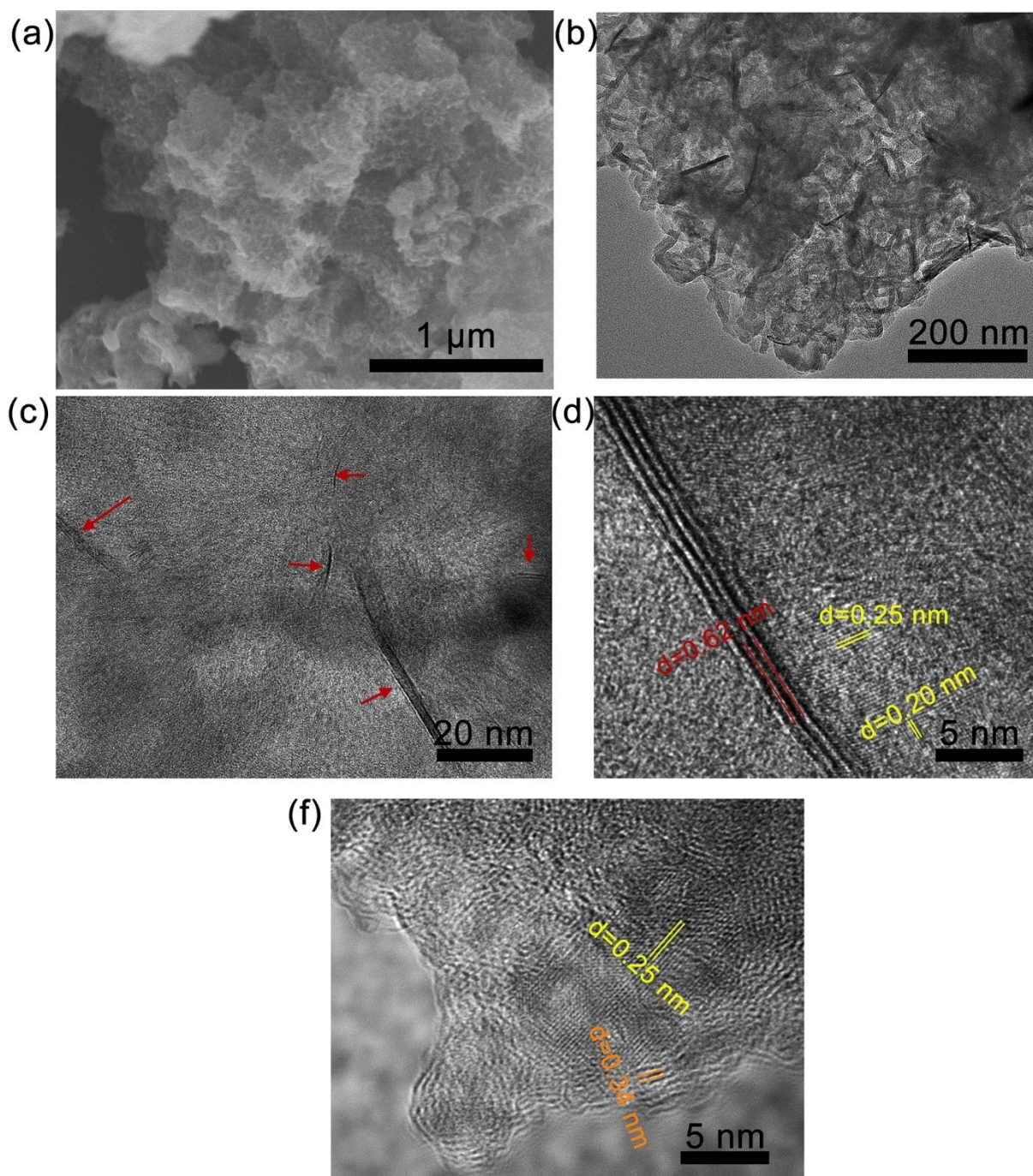


Figure S22. (a) SEM, (b) low-magnification TEM, (c) high-magnification TEM, and (d) high-resolution TEM images of CoS/WS₂/CNC-1-ADT. The lattice fringes at a distance of 0.34 nm is indexed to the (002) planes of graphite.

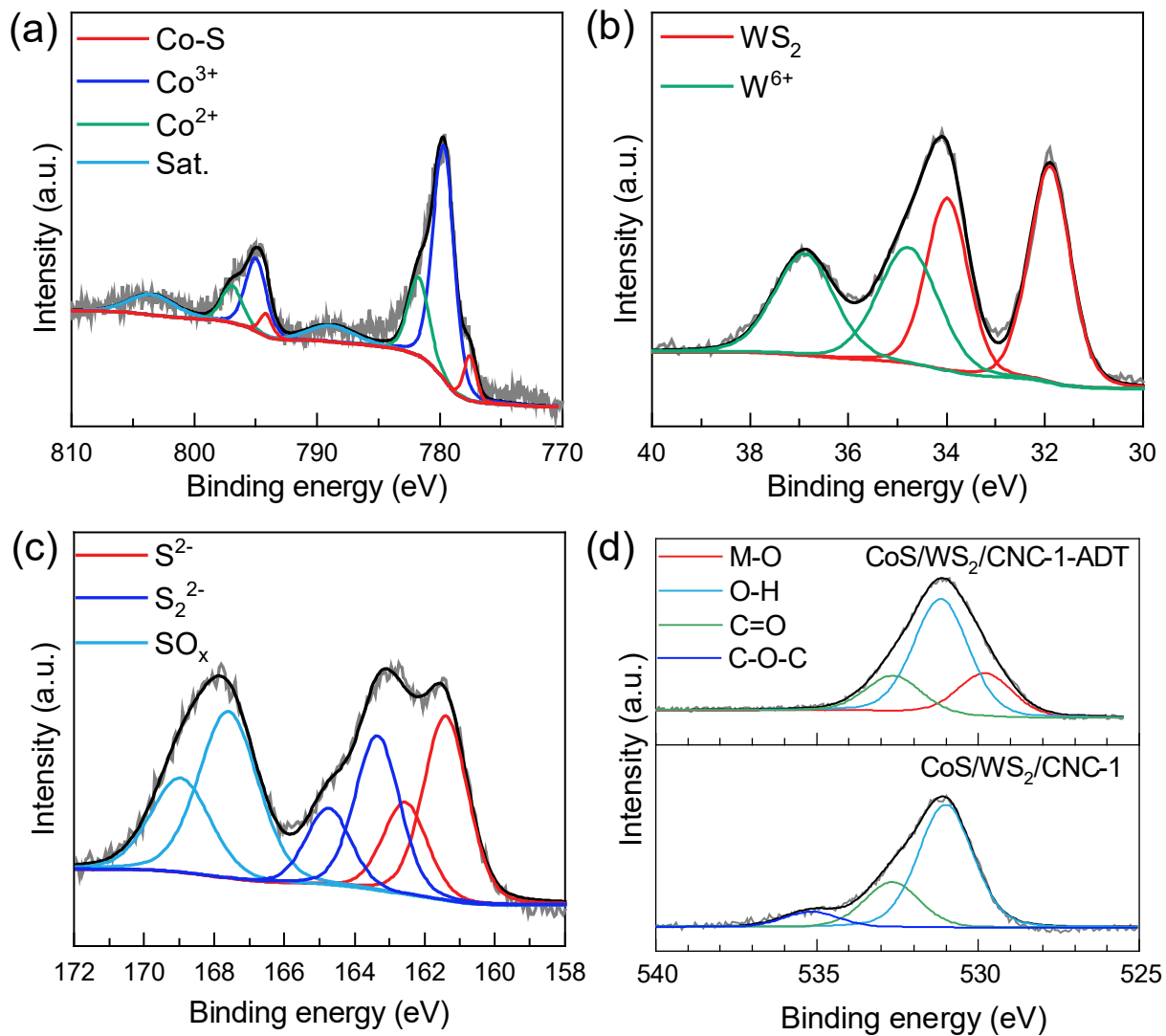


Figure 23. High-resolution (a) Co 2p, (b) W 4f, (c) S 2p, and (d) O 1s XPS spectra of CoS/WS₂/CNC-1-ADT.

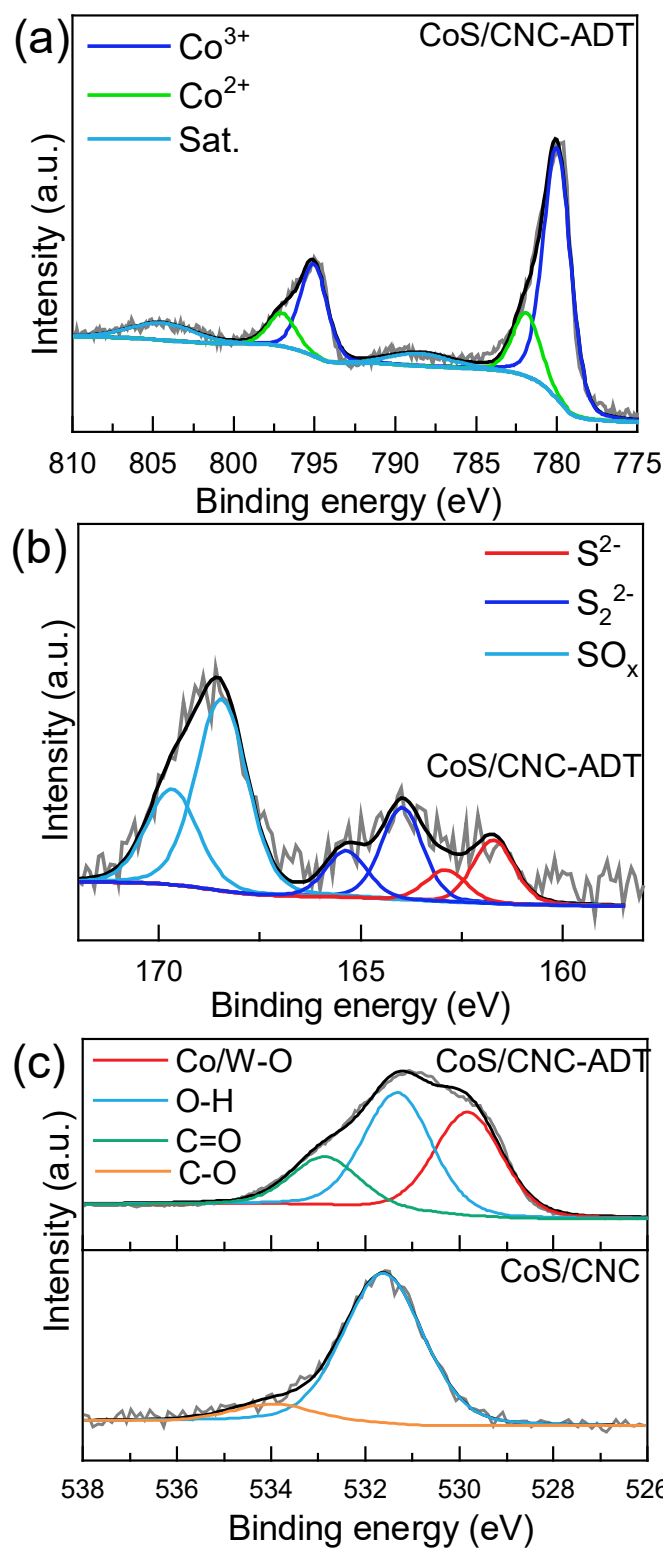


Figure S24. High-resolution (a) Co 2p, (b) S 2p, and (c) O 1s XPS spectra of CoS/CNC and CoS/CNC-ADT.

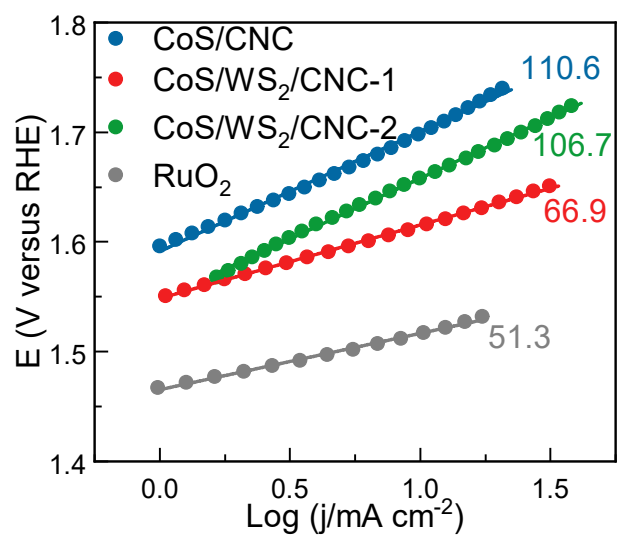


Figure S25. Tafel curves of CoS/CNC, CoS/WS₂/CNC-1, CoS/WS₂/CNC-2, and RuO₂ catalysts.

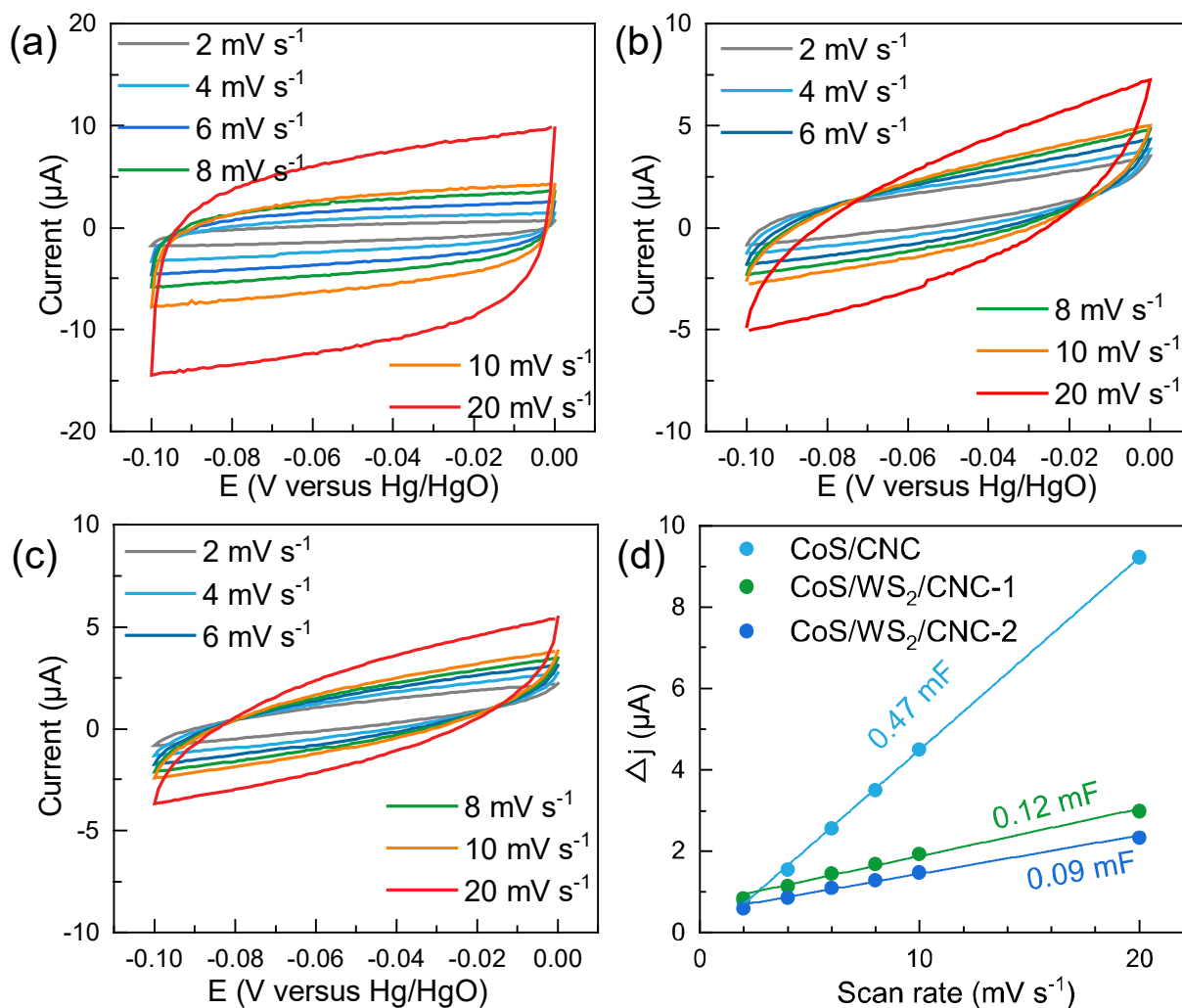


Figure S26. CV curves of (a) CoS/CNC, (b) CoS/WS₂/CNC-1, and (c) CoS/WS₂/CNC-2 recorded in N₂-saturated 1.0 M KOH solution at 2-20 mV s⁻¹, and (d) corresponding non-faradaic current at -0.05 V versus Hg/HgO versus scan rate. The non-faradaic current is suggested to be originated from double-layer charging, and thus the electrochemically active surface area (*ECSA*) can be derived from the double-layer capacitance (*C_{dl}*) according to the equations 7 and 8:

$$C_{dl} = i_c / \nu \quad [8]$$

$$ECSA = C_{dl} / C_s \quad [9]$$

Where *i_c* is the non-faradaic current at -0.05 V versus Hg/HgO, *ν* is the scan rate (mV s⁻¹), and *C_s* is a general capacity (40 μF cm⁻²).

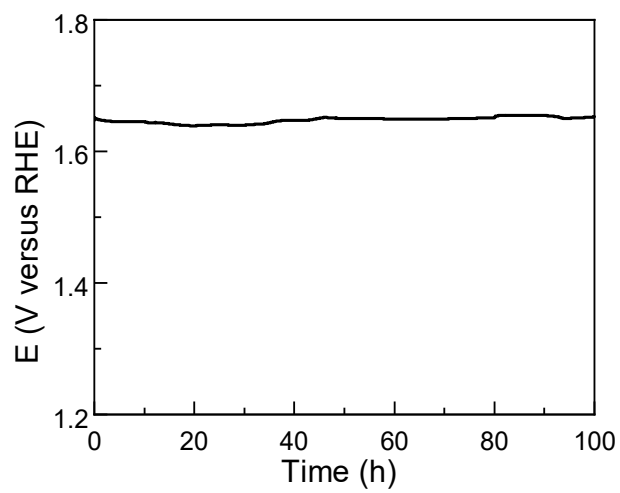


Figure S27. Chronopotentiometric response of CoS/WS₂/CNC-1 catalyst at a current density of 20 mA cm⁻².

Table S1. The cobalt content (wt%) and cobalt/tungsten (Co/W) molar ratio in the CoS/CNC, CoS/WS₂/CNC-1, and CoS/WS₂/CNC-2 determined using microwave-plasma atomic emission spectroscopy (MP-AES) and X-ray fluorescence (XRF).

$n_{HCO_3^-} : n_{WO_4^{2-}}$	Precursors	Co ^a	Co/W ^b	Samples
8:0	ZIF-67/ <i>Pm</i> AP-HCO ₃ ⁻	20.2	N/A	CoS/CNC
4:2	ZIF-67/ <i>Pm</i> AP-HCO ₃ ⁻ /WO ₄ ²⁻	19.6	9.8	CoS/WS ₂ /CNC-1
0:4	ZIF-67/ <i>Pm</i> AP-WO ₄ ²⁻	18.7	6.2	CoS/WS ₂ /CNC-2

^a: The cobalt percentage (wt%) in the samples is carried out on MP-AES.

^b: The Co/W molar ratio in the samples is performed on XRF.

Table S2. Comparison of OER and ORR activities including half-wave potential ($E_{1/2}$ vs. RHE), peak power density (PPD, mW cm^{-2}) and stability (h, mA cm^{-2}) of rechargeable zinc-air batteries between XX catalysts and precisely reported transition-metal sulfide catalysts.

Catalysts	$E_{1/2}$	PPD	stability	Ref.
CoS/WS₂/CNC-1	0.868	183.5	480 (5 mA cm⁻²)	This work
NiS ₂ /CoS ₂ -O NWs	0.7	N/A	30 (5 mA cm ⁻²)	1
NiFeS ₂ /S-GO	0.74	~ 50	60 (10 mA cm ⁻²)	2
NiCo ₂ S ₄ /N-CNT	0.8	147	16 (10 mA cm ⁻²)	3
NiCo ₂ S ₄ @g-C ₃ N ₄ -CNT	0.76	142	110 (10 mA cm ⁻²)	4
Co _{9-x} Ni _x S ₈ /NC	0.86	75	60 (10 mA cm ⁻²)	5
Co ₃ FeS _{1.5} (OH) ₆	0.721	113	36 (2 mA cm ⁻²)	6
CoIn ₂ S ₄ /S-rGO	0.83	133	50 (10 mA cm ⁻²)	7
Co-NC@CoFeS ₂	0.805	174	130 (10 mA cm ⁻²)	8
Co ₉ S ₈ -MoS ₂	0.82	222	50 (5 mA cm ⁻²)	9
Co ₂ Cu ₁ -S	0.82	195	80 (3.0 mA cm ⁻²)	10
Co ₃ Fe ₁ S ₂	0.868	387	70 (10 mA cm ⁻²)	11
NiCo ₂ S ₄ /ZnS	0.8	160	130 (5 mA cm ⁻²)	12
CoNiFe-S MNs	0.78	140	40 (2 mA cm ⁻²)	13
CuCo ₂ S ₄ NSs@N-CNFs	0.821	232	100 (5 mA cm ⁻²)	14
FeCoMoS@NG	0.83	118	70 (2 mA cm ⁻²)	15

References

1. J. Yin, Y. Li, F. Lv, M. Lu, K. Sun, W. Wang, L. Wang, F. Cheng, Y. Li, P. Xi and S. Guo, *Adv. Mater.*, 2017, **29**, 1704681.
2. D. Zhou, Y. Jia, H. Yang, W. Xu, K. Sun, J. Zhang, S. Wang, Y. Kuang, B. Liu and X. Sun, *J. Mater. Chem. A*, 2018, **6**, 21162-21166.
3. X. Han, X. Wu, C. Zhong, Y. Deng, N. Zhao and W. Hu, *Nano Energy*, 2017, **31**, 541-550.
4. X. Han, W. Zhang, X. Ma, C. Zhong, N. Zhao, W. Hu and Y. Deng, *Adv. Mater.*, 2019, **31**, 1808281.
5. Z. Cai, I. Yamada and S. Yagi, *ACS Appl. Mater. Interfaces*, 2020, **12**, 5847-5856.
6. H.-F. Wang, C. Tang, B. Wang, B. Q. Li and Q. Zhang, *Adv. Mater.*, 2017, **29**, 1702327.
7. G. Fu, J. Wang, Y. Chen, Y. Liu, Y. Tang, J. B. Goodenough and J. M. Lee, *Adv. Energy Mater.*, 2018, **8**, 1802263.
8. Y. Wang, W. Jin, C. Xuan, J. Wang, J. Li, Q. Yu, B. Li, C. Wang, W. Cai and J. Wang, *J. Power Sources*, 2021, **512**, 230430.
9. W. Zhang, X. Zhao, Y. Zhao, J. Zhang, X. Li, L. Fang and L. Li, *ACS Appl. Mater. Interfaces*, 2020, **12**, 10280-10290.
10. L. Zhuang, H. Tao, F. Xu, C. Lian, H. Liu, K. Wang, J. Li, W. Zhou, Z. Xu, Z. Shao and Z. Zhu, *J. Mater. Chem. A*, 2021, **9**, 18329-18337.
11. M. Kumar and T. C. Nagaiah, *J. Mater. Chem. A*, 2022, **10**, 4720-4730.
12. J. Sun, H. Xue, N. Guo, T. Song, Y.-r. Hao, J. Sun, J. Zhang and Q. Wang, *Angew. Chem. Int. Ed.*, 2021, **60**, 19435-19441.
13. H. Yang, B. Wang, H. Li, B. Ni, K. Wang, Q. Zhang and X. Wang, *Adv. Energy Mater.*, 2018, **8**, 1801839.

14. Z. Pan, H. Chen, J. Yang, Y. Ma, Q. Zhang, Z. Kou, X. Ding, Y. Pang, L. Zhang, Q. Gu, C. Yan and J. Wang, *Adv. Sci.*, 2019, **6**, 1900628.
15. S. Ramakrishnan, J. Balamurugan, M. Vinothkannan, A. R. Kim, S. Sengodan and D. J. Yoo, *Appl. Catal. B Environ.*, 2020, **279**, 119381.